



PERGAMON

International Journal of Impact Engineering 25 (2001) 887–910

INTERNATIONAL  
JOURNAL OF  
**IMPACT  
ENGINEERING**

www.elsevier.com/locate/ijimpeng

## Dynamic behavior of concrete at high strain rates and pressures: II. numerical simulation

S.W. Park<sup>1</sup>, Q. Xia, M. Zhou\*

*The George W. Woodruff School of Mechanical Engineering, Georgia Institute of Technology, Atlanta,  
GA 30332-0405, USA*

Received 1 June 1999; received in revised form 16 October 1999; accepted 6 April 2001

---

### Abstract

The response of concrete and mortar under high-strain-rate impact loading are analyzed using fully dynamic finite element simulations. The analyses concern the load-carrying capacity, energy absorbency and the effect of the microstructure. The simulations focus on the plate impact configuration used in the experimental part of this research, allowing for direct comparison of model predictions with experimental measurements. A micromechanical model is formulated and used, accounting for the two-phase composite microstructure of concrete. Arbitrary microstructural phase morphologies of actual concrete used in impact experiments are digitized and explicitly considered in the numerical models. The behavior of the two constituent phases in the concrete are characterized by an extended Drucker–Prager model that accounts for pressure-dependence, rate-sensitivity, and strain hardening/softening. Model parameters are determined by independent impact experiments on mortar and through a parametric study in which the prediction of numerical simulations is matched with measurements from experiments on concrete and mortar. Calculations show that significant inelastic deformations occur in the mortar matrix under the impact conditions analyzed and relatively smaller inelastic strains are seen in the aggregates. The influence of aggregate volume fraction on the dynamic load-carrying capacity of concrete is explored. The strength increases with aggregate volume fraction and an enhancement of approximately 30% over that of mortar is found for an aggregate volume fraction of 42%. Numerical simulations also show increasing energy absorbency with increasing aggregate volume fraction and provide a time-resolved characterization for the history of work dissipation as the deformation progresses. © 2001 Elsevier Science Ltd. All rights reserved.

*Keywords:* Concrete; Dynamic behavior; Constitutive model; Numerical simulation; Micromechanical model; Stress-carrying capacity; Energy absorbency

---

\*Corresponding author. Tel.: +1-404-894-3294; fax: +1-404-894-0186.

*E-mail address:* min.zhou@me.gatech.edu (M. Zhou).

<sup>1</sup>Currently, U.S. Federal Highway Administration, TFHRC/HRDI/PSI, 6300 Georgetown Pike, McLean, VA 22101, USA.

## Nomenclature

$c$	longitudinal wave speed
$\mathbf{D}$	rate of deformation tensor
$\mathbf{D}^e$	elastic part of rate of deformation tensor
$\mathbf{D}^p$	plastic part of rate of deformation tensor
$\mathbf{F}$	deformation gradient tensor
$\mathbf{F}^e$	elastic part of deformation gradient tensor
$\mathbf{F}^p$	plastic part of deformation gradient tensor
$F$	scalar yield function
$G$	plastic potential
$J$	Jacobian determinant ( $= \det \mathbf{F} $ )
$\mathbf{L}$	fourth-order elastic modulus tensor
$p$	pressure
$\mathbf{u}$	displacement vector
$\dot{\mathbf{u}}$	particle velocity vector
$V_0$	impact velocity
$V_{fs}$	free surface velocity of anvil plate
$W^e$	elastic strain energy density
$W^p$	plastic work density
$\beta$	internal friction angle
$\bar{\epsilon}^p$	equivalent plastic strain
$\dot{\bar{\epsilon}}^p$	equivalent plastic strain rate
$\rho$	mass density
$\boldsymbol{\sigma}$	Cauchy stress tensor
$\boldsymbol{\sigma}'$	deviatoric stress tensor
$\bar{\sigma}$	Mises equivalent stress
$\mu$	coefficient of friction
$\boldsymbol{\tau}$	Kirchhoff stress tensor
$\hat{\boldsymbol{\tau}}$	Jaumann rate of Kirchhoff stress tensor
$\psi$	dilation angle
$\Omega^p$	total plastic work

## 1. Introduction

The design of concrete structures to sustain extreme loading conditions from blast or projectile penetration requires the characterization of the material behavior under relevant conditions and material models that can be used computationally for simulation and analysis. The lack of data and such constitutive models for concrete has posed a significant challenge to structure designers and material engineers.

Concrete is a two-phase composite comprising mortar and aggregate. The aggregate serves as a reinforcement and increases the effective strength and stiffness of the overall composite. When

concrete is subjected to dynamic loading of sufficient magnitudes, a series of deformation and failure events occur. The entire process may consist of initial elastic deformation, microcracking, fragmentation, rubblization and post-rubblization flow. The development of constitutive models capable of describing the complex deformation and failure mechanisms under dynamic conditions is a challenging task. A successful model should account for such effects as modulus degradation from microcracking, pressure-dependent shear strength, post-failure strain softening, and strain-rate sensitivity. Distributed microcracking and plastic flow are the primary damage mechanisms followed by localization which leads to global failure of many brittle materials such as rocks, concrete, ceramics and ceramic matrix composites [1,2]. Weakening of materials due to distributed damage is normally modeled using constitutive theories based on a continuum framework. Even localized damage in concrete has been handled using averaging or smearing approaches within the framework of continuum theories [3,4].

The responses of concrete structures under impact loading have been analyzed numerically by a number of groups. Different types of constitutive laws have been used. For example, Beshara and Virdi [5] analyzed reinforced concrete structures subjected to impulsive loading using a constitutive law which models the compressive behavior of concrete as elasto-viscoplastic and the tensile behavior as linear-elastic/strain-softening. This model incorporated features of the rate-dependent model for compression developed by Soroushian et al. [6]. Later on, Beshara [7] used the smeared crack approach to model the tensile behavior of concrete. Shirai et al. [8] conducted numerical studies of missile impact on reinforced concrete using a material model that accounts for the effects of strain rate. Tedesco et al. [9,10] derived a rate-dependent constitutive model for concrete using a regression analysis of data from split Hopkinson pressure bar (SHPB) tests and incorporated their model into a general-purpose finite element code. Moxley et al. [11] studied the interaction between thin-walled steel projectiles and concrete targets under high-velocity impact through experiments and numerical analysis. Their numerical work used a rigid-body penetration trajectory code developed by Berger and Adley [12]. Forrestal and Tzou [13] developed a cavity-expansion penetration model for concrete targets, accounting for the pressure-dependent shear strength of concrete. Cela [14] used an elasto-viscoplastic concrete model to analyze the behavior of reinforced concrete structures subjected to dynamic loads. Recently, techniques based on the discrete element method have been used to simulate the evolution of damage in concrete structures subjected to impulsive loading from various sources [15–17].

Many of these material models are extensions of the classical theory of plasticity in a framework suitable for describing key features of the dynamic behavior of concrete. For example, Forrestal and Tzou [13] used the Mohr–Coulomb failure criterion and Cela [14] used the Drucker–Prager model to simulate the rate-independent part of the inelastic deformation of concrete. Cela [14] then introduced an *a posteriori* correction scheme to account for the rate-dependent part of the inelastic deformation. In numerical implementations, general-purpose finite element codes are frequently used in combination with specifically designed material models. For example, Shirai et al. [8] used DYNA-3D, Tedesco et al. [9,10] developed a rate-dependent concrete model for ADINA, and Moxley et al. [11] implemented the penetration model by Berger and Adley [12] in ABAQUS. Although these studies all concern the dynamic response of concrete structures, they do not deal with the very high strain rates (above  $10^4 \text{ s}^{-1}$ ) and high hydrostatic pressures found in actual impact and penetration events. For instance, the analysis of Beshara and Virdi [5] concerned only strain rates of up to  $10 \text{ s}^{-1}$ . The problems analyzed by Shirai et al. [8]

involved only impact velocities between 5 and 10 ms<sup>-1</sup>. And the model of Tedesco et al. [9,10] are based on data for strain rates of up to 10<sup>3</sup> s<sup>-1</sup>. Furthermore, existing models do not allow the effect of concrete microstructure to be explicitly analyzed.

In the experimental part of this investigation, a series of experiments have been carried out to provide data on the behavior of a G-mix concrete and mortar over the strain rate range of 10<sup>-3</sup>–10<sup>4</sup> s<sup>-1</sup> [18]. The focus of the experiments is on the part of the behavior at strain rates above 10<sup>3</sup> s<sup>-1</sup> and under hydrostatic pressures of up to 1.5 GPa. This paper presents a micromechanical model for the concrete. The formulation of the model is based on the results of the experiments. A fully dynamic, finite deformation framework of analysis is used. A series of numerical simulations of the impact experiments reported by Grote et al. [18] are carried out. The analysis concerns the time-resolved response of concrete and mortar at strain rates on the order of 10<sup>4</sup> s<sup>-1</sup> and confining pressures above 1 GPa. The simulation focuses on the evolution of dynamic load-carrying capacity and energy absorbency of concrete during early stages of the impact deformation, since the load-carrying capacity is usually the highest in the earliest stages of deformation and is dictated by elastoplastic response, granular flow and fragmentation. The simulations are not carried out into late stages of deformation when rubbleization and post-rubbleization flow are the dominant processes. The analysis also addresses issues such as the magnitude and effect of the hydrostatic pressures that develop as a result of lateral inertial confinement. The micromechanical model provides an explicit account for the microstructural morphologies of the mortar and aggregate phases in concrete. The model incorporates the arbitrary phase distributions of actual concrete specimens used in the experiments, allowing the effects of phase distribution and phase volume fraction to be explored. A series of random samples of the concrete microstructure is shown in Fig. 1. The behaviors of the constituents are characterized by an extended Drucker–Prager model, and the numerical modeling is conducted using the ABAQUS/Explicit finite element package.

## 2. Framework of analysis

A fully dynamic finite element model is formulated to simulate the response of concrete and mortar under conditions of the plate impact experiments. To account for the finite strains in the deformation, a Lagrangian finite deformation formulation is used. The independent variables are the position of a material point in the reference configuration ( $\mathbf{x}$ ) and time ( $t$ ). Relative to a fixed Cartesian frame, a material point initially at  $\mathbf{x}$  occupies position  $\bar{\mathbf{x}}$  in the current configuration. The displacement vector and the deformation gradient are defined as  $\mathbf{u} = \bar{\mathbf{x}} - \mathbf{x}$  and  $\mathbf{F} = \partial\bar{\mathbf{x}}/\partial\mathbf{x}$ , respectively. The dynamic principle of virtual work specifies balance of momentum,

$$\int_V \boldsymbol{\tau} : \delta\mathbf{D} \, dV = \int_S \mathbf{T}\delta\dot{\mathbf{u}} \, dS - \int_V \rho \frac{\partial^2 \mathbf{u}}{\partial t^2} \delta\dot{\mathbf{u}} \, dV, \quad (1)$$

where  $V$ ,  $S$  and  $\rho$  are the volume, surface and mass density, respectively, of a body in the reference configuration.  $\boldsymbol{\tau} = J\boldsymbol{\sigma} = \det|\mathbf{F}|\boldsymbol{\sigma}$  is the Kirchhoff stress, with  $\boldsymbol{\sigma}$  being the Cauchy stress.  $\mathbf{T}$  is the traction vector,  $\mathbf{D}$  denotes the rate of deformation tensor, and  $\dot{\mathbf{u}}$  denotes  $\partial\mathbf{u}/\partial t$ . Also,  $\delta\mathbf{D}$  and  $\delta\dot{\mathbf{u}}$  denote admissible variations in  $\mathbf{D}$  and  $\dot{\mathbf{u}}$ , respectively, and scalar product  $\boldsymbol{\tau} : \delta\mathbf{D} = \tau_{ij}\delta\mathbf{D}_{ij}$ .

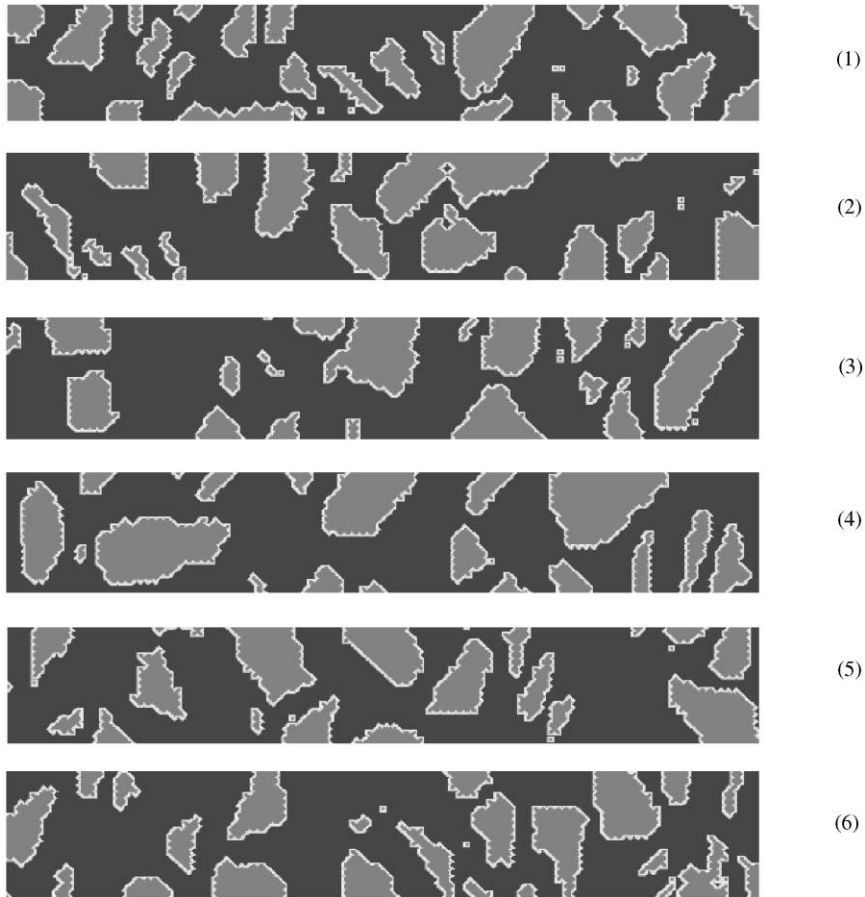


Fig. 1. Different concrete microstructures, having the same aggregate volume fraction, considered in the study. (The light contrast represents aggregate.)

For elastic–plastic materials, deformation gradient  $\mathbf{F}$  can be decomposed into an elastic part  $\mathbf{F}^e$  and a plastic part  $\mathbf{F}^p$  through

$$\mathbf{F} = \mathbf{F}^e \cdot \mathbf{F}^p. \quad (2)$$

Under the conditions of small elastic deformations, this multiplicative decomposition of  $\mathbf{F}$  implies an additive decomposition of the rate of deformation  $\mathbf{D}$  into an elastic part and a plastic part, i.e.

$$\mathbf{D} = \mathbf{D}^e + \mathbf{D}^p, \quad (3)$$

where  $\mathbf{D}$  is the symmetric part of  $\partial \dot{\mathbf{u}} / \partial \bar{\mathbf{x}}$ . The incremental stress–strain relations is written as

$$\hat{\boldsymbol{\tau}} = \mathbf{L} : (\mathbf{D} - \mathbf{D}^p), \quad (4)$$

with  $\hat{\boldsymbol{\tau}}$  being the Jaumann rate of Kirchhoff stress and  $\mathbf{L}$  the fourth-order elasticity tensor. The plastic part of the rate of deformation  $\mathbf{D}^p$  describes the granular flow of the materials after the

onset of damage. This part of the behavior is characterized by an extended Drucker–Prager model, as discussed below.

### 2.1. Constitutive laws

The behavior of concrete is complex due to an array of morphological features as well as deformation and failure mechanisms inherent in the concrete microstructure. The complicating factors include heterogeneous constitution, random phase distribution, arbitrary microcrack patterns, and internal granular friction. The complexity of the microscopic processes renders explicit resolution of the influences a highly challenging task. Simplification is possible if one is willing to focus on the behavior of the mortar and the aggregate phases as ensembles of granules. On the continuum level, the most important characteristic of the inelastic flow of granular materials is the pressure dependence of flow strength [1,19]. Therefore, a phenomenological approach is taken in the current work. Specifically, an extended Drucker–Prager model is used to characterize the behavior of mortar and aggregate. This model is chosen because of its ability to provide phenomenological account for pressure-dependent flow due to internal friction while allowing the evolution of the deformation to be tracked through strain hardening and strain softening within the framework of finite deformation kinematics. The model is implemented in a strain-rate sensitive framework, allowing dynamic, high strain rate behavior to be analyzed. The original Drucker–Prager plasticity model [20] has been extended to finite strain regimes by, e.g., Hofstetter and Taylor [21] and Famiglietti and Prevost [22] without strain rate effects.

It is important to point out that granular materials or cracked concrete have been shown to exhibit slip-induced dilatancy [23,24]. The volume change associated with this effect is usually very small under high pressures. This effect is not explicitly modeled since the hydrostatic pressures considered here are on the order of 1–1.5 GPa and dominate volume change as well as shear strength of the materials.

#### 2.1.1. Yield criterion

The extended Drucker–Prager model used has a linear yield criterion, i.e.

$$F = \tau - p \tan \beta - d = 0, \quad (5)$$

where  $\beta$  is the internal friction angle of the material in the meridional (or  $p - \tau$ ) stress plane,  $d$  is the yield stress under pure shear,  $\tau$  is a deviatoric stress measure defined as

$$\tau = \frac{1}{2} \bar{\sigma} \left[ 1 + \frac{1}{K} - \left( 1 - \frac{1}{K} \right) \frac{r^3}{\bar{\sigma}^3} \right] \quad (6)$$

and

$$p = -\frac{1}{3} \text{tr}(\boldsymbol{\sigma}) \quad (7)$$

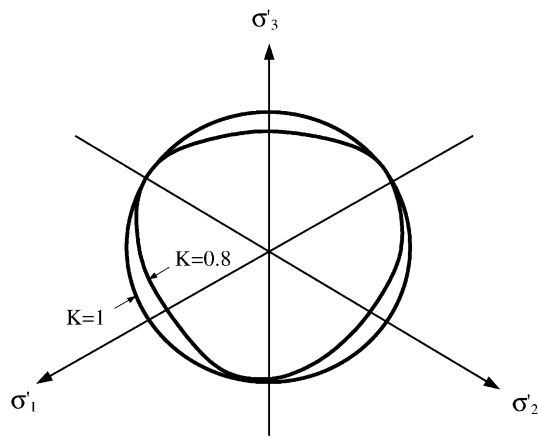
is the pressure. In Eq. (6),

$$\bar{\sigma} = \sqrt{\frac{3}{2} \boldsymbol{\sigma}' : \boldsymbol{\sigma}'} \quad (8)$$

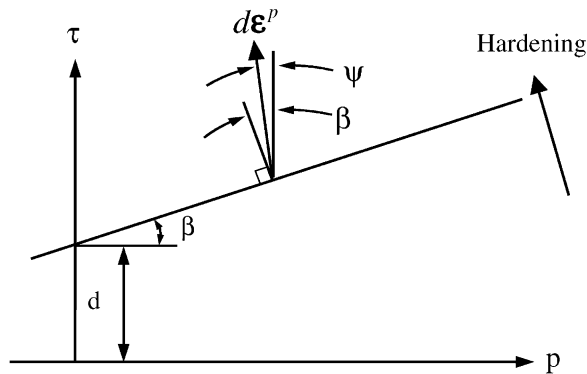
is the Mises equivalent stress and  $r^3$  is the third invariant of the deviatoric stress tensor defined as

$$r^3 = \frac{9}{2} \boldsymbol{\sigma}' : \boldsymbol{\sigma}' \cdot \boldsymbol{\sigma}' \tag{9}$$

with  $\boldsymbol{\sigma}' \equiv \boldsymbol{\sigma} + p\mathbf{I}$  being the deviatoric stress tensor. In Eqs. (8) and (9),  $\boldsymbol{\sigma}' : \boldsymbol{\sigma}' = \sigma'_{ij}\sigma'_{ij}$  and  $(\boldsymbol{\sigma}' \cdot \boldsymbol{\sigma}')_{ij} = \sigma'_{ik}\sigma'_{kj}$ , where repeated indices imply summation over their range. The deviatoric stress measure  $\tau$  accounts for different responses under tension and compression through the parameter  $K$  which varies within the range of  $0.778 \leq K \leq 1.0$  to ensure the convexity of the yield surface. When  $K=1$ , the dependence on the third deviatoric stress invariant is removed and the original Drucker–Prager model [20] is recovered. Further, when  $K=1$  and  $\beta = 0$ , the condition simplifies to the von Mises yield criterion. The yield surface described by Eqs. (5) and (6) is schematically illustrated in Fig. 2(a) in the deviatoric plane and in Fig. 2(b) in the meridional stress plane. The



(a) In the deviatoric plane



(b) In the meridional plane

Fig. 2. A schematic illustration of the yield surface, flow and hardening directions in the extended Drucker–Prager model.

slope of the yield surface,  $\tan \beta$ , in Fig. 2(b) indicates the effects of hydrostatic pressure on the yield strength of the material. The angle  $\beta$  is often related to the angle of internal friction under a specific loading condition. For instance, under triaxial compression [19],

$$\tan \beta = \frac{6 \sin \phi}{3 - \sin \phi}, \quad (10)$$

where  $\phi$  is the angle of internal friction obtained from a triaxial compression test. The angle  $\phi$  is usually used in the Mohr–Coulomb yield criterion.

### 2.1.2. Flow rule

Potential flow is assumed in the extended Drucker–Prager model, i.e.

$$\mathbf{D}^p = \frac{\dot{\bar{\epsilon}}^p}{c} \frac{\partial G}{\partial \boldsymbol{\sigma}}, \quad (11)$$

where  $c$  is a constant defined as

$$c = 1 - \frac{1}{3} \tan \psi, \quad (12)$$

$\mathbf{D}^p$  is the plastic part of the rate of deformation, and  $\dot{\bar{\epsilon}}^p$  is the equivalent plastic strain rate satisfying the plastic consistency condition such that  $\bar{\sigma} \dot{\bar{\epsilon}}^p = \boldsymbol{\sigma} : \mathbf{D}^p$ . Together with Eq. (8), this yields

$$\dot{\bar{\epsilon}}^p = \sqrt{\frac{2}{3} \mathbf{D}^p : \mathbf{D}^p}. \quad (13)$$

The scalar quantity  $G$  in Eq. (11) is a flow potential defined as

$$G = \tau - p \tan \psi, \quad (14)$$

where  $\psi$  is the dilation angle whose geometrical interpretation is shown in Fig. 2(b). The model indicates nonassociated flow in the  $p$ – $\tau$  plane and associated flow in the deviatoric plane. When  $\psi = \phi$ , a fully associated flow rule as used in the original Drucker–Prager model is recovered. If  $\psi = 0$ , the inelastic deformation is incompressible.

### 2.1.3. Strain hardening/softening and rate-sensitivity

Microcracking contributes to reducing the strength and modulus of mortar and concrete. The modulus degradation due to microcrack growth prior to the peak stress is modeled as strain hardening in the inelastic portion of the constitutive relation. Mortar and concrete exhibit strain hardening up to the peak stress followed by strain softening. The extended Drucker–Prager model permits isotropic hardening and/or softening to be accounted for during loading. In the analyses reported, the uniaxial stress–strain relations obtained from Hopkinson bar experiments are used to determine the hardening and softening behavior of the materials. The rate dependence of flow stress is accounted for by scaling the quasistatic flow stress. Specifically,

$$\bar{\sigma} = R(\dot{\bar{\epsilon}}) \sigma_0, \quad (15)$$

where  $\bar{\sigma}$  is the dynamic flow stress at a given strain rate and  $\sigma_0$  is the quasistatic flow stress at a strain rate of  $10^{-3} \text{ s}^{-1}$ . The scale factor  $R$  is a function of strain rate and is determined from experiments conducted at different strain rates [18].

## 2.2. Problem analyzed

Responses of concrete and mortar specimens subjected to plate impact are simulated numerically. A schematic illustration of the plate impact configuration analyzed is shown in Fig. 3. The details of the plate impact configuration are available in the companion paper [18]. Finite element discretization of the material microstructure explicitly accounts for the distributions of the mortar and aggregate phases in concrete. To this end, micrographs of random samples of the microstructure of concrete are digitized and used in the numerical modeling. The discrete finite element mesh resolves the microstructural morphologies of the phases. An element assumes the properties of either the mortar or the properties of the aggregate. If the centroid of the element falls inside the mortar, it is assigned the properties of the mortar. Otherwise, it is assigned the properties of the aggregate. Six different microstructures, as shown in Fig. 1, are considered. These microstructures, randomly chosen from digitized micrographs of actual concrete specimens prior to the experiments by Grote et al. [18], have quite different and arbitrary distributions of mortar and aggregate. They all have the same aggregate volume fraction of 42%, reflecting the aggregate volume fraction of concrete samples tested in the experiments.

The finite element mesh used in the simulations is shown in Fig. 4. The microstructure used is (4) in Fig. 1. The dark areas in the concrete specimen (Fig. 4) represent aggregate. Three-node triangular plane-strain elements are used for the specimen and four-node quadrilateral plain-strain elements are used for the steel target. The actual mesh used in the calculations has 7380 elements and 6194 nodes (or 12,388 degrees of freedom). Finer meshes with 4 times as many elements were also used to conduct the simulation, but no significant difference was observed between the results obtained using the different mesh sizes.

## 2.3. Initial and boundary conditions

The impact process is explicitly simulated. The specimen is flying at a velocity of  $V_0$  and the anvil target is at rest initially. Both plates are stress-free prior to impact. All external surfaces of

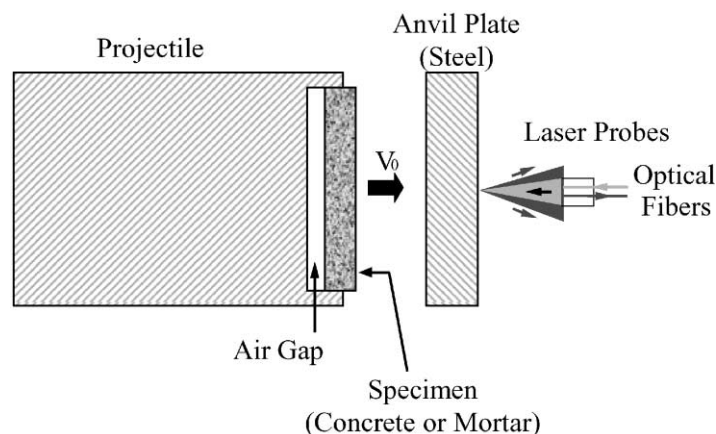


Fig. 3. A schematic illustration of the plate impact configuration.

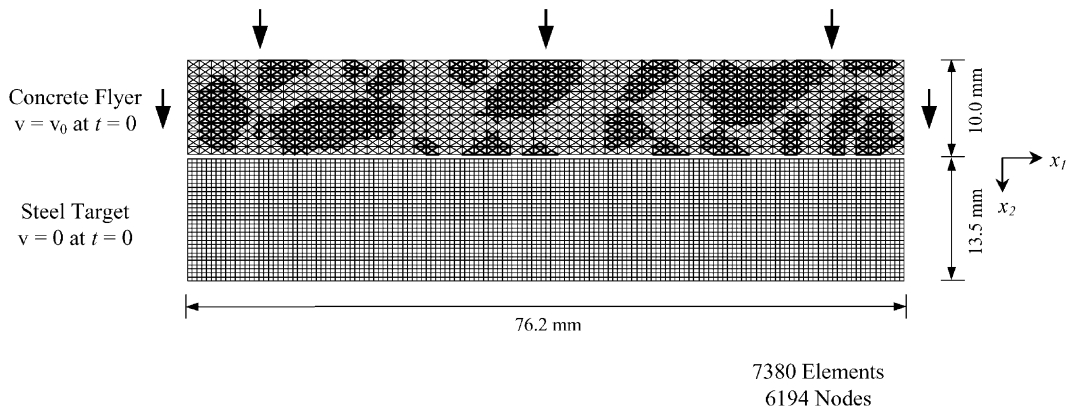


Fig. 4. An illustration of the finite element mesh and impact configuration used in numerical simulations.

the specimen and the anvil plate are traction-free except for the impact faces which remain in contact for most of the impact process. A friction model is employed for the interface between the specimen and anvil plate. The contact between the specimen and the anvil plate is assumed to follow the isotropic Coulomb law of friction, i.e.

$$\tau_{cr} = \mu N, \quad (16)$$

where  $\tau_{cr}$  is the critical shear stress at which sliding between the surfaces occurs,  $N$  is the normal contact pressure between the surfaces, and  $\mu$  is the coefficient of friction which is taken to be 0.3 in the analyses.

#### 2.4. Calibration of model parameters

The parameters in the constitutive model are determined using the experimental data reported in [18] wherever possible. The parameters that cannot be determined directly from the experimental data, including the friction angle  $\beta$ , dilation angle  $\psi$  and the ratio  $K$ , are chosen through a parametric study in which numerical predictions with assumed values for the parameters are matched with experimental observations. Specifically, a series of calculations are carried out for the independent plate impact experiments reported in [18]. The particular quantity used in the comparison is the time history of the free surface velocity at the center of the anvil plate. This quantity is used because (1) it is measured directly during the impact experiments using a velocity interferometer system for any reflector (VISAR), and (2) according to the one-dimensional elastic stress wave theory, stresses in the elastic target plate are directly related to this surface velocity. The latter provides a means for the measured velocity to be interpreted as the average stress carried by the specimen material during an impact experiment. Specifically, since the target (or anvil) plate in Fig. 3 remains linear elastic,

$$\sigma(t) = \frac{1}{2}\rho c V_{fs}(t), \quad (17)$$

where  $\sigma(t)$  is the average stress,  $\rho$  is the mass density of the target material,  $c$  is the longitudinal wave speed in the target material, and  $V_{fs}(t)$  is the free surface velocity at the center of the target plate.

The calibration process consists of two stages. The first stage is to calibrate the material parameters for mortar using plate impact experiments conducted on mortar. The second stage concerns the determination of material parameters for aggregate using plate impact experiments conducted on concrete. In the second stage, the material parameters for mortar already determined in stage one are used. In the parametric studies, each of the parameters is varied systematically and independently over its possible range to analyze its effect on the predicted behavior. By considering combinations of parametric values and comparing the predicted responses with experimental observations, a set of optimal values are identified for the parameters.

Fig. 5 shows the analysis and result of the parametric study for mortar. Calculated free surface velocity profiles are shown in Fig. 5(a)–(c) for an experiment with an impact velocity of  $290 \text{ ms}^{-1}$ . The calculated profiles corresponding to three different values of  $\beta$  ( $15^\circ$ ,  $25^\circ$ ,  $50^\circ$ ) with  $\psi = 20^\circ$  and  $K = 0.8$  are shown in Fig. 5(a). Note that the free surface velocity shown is proportional to the average stress at the specimen/target interface through Eq. (17). Higher velocity corresponds to higher stresses in the specimen. It can be seen that increasing the friction angle  $\beta$  (i.e., increasing internal friction) strengthens the material. The effect of the dilation angle  $\psi$  on the velocity profile is shown in Fig. 5(b). The profiles are for three different values of  $\psi$  ( $5^\circ$ ,  $20^\circ$  and  $30^\circ$ ) with  $\beta = 30^\circ$  and  $K = 0.8$ . This parameter has a similar effect as the friction angle  $\beta$ . In Fig. 5(c), the profiles for

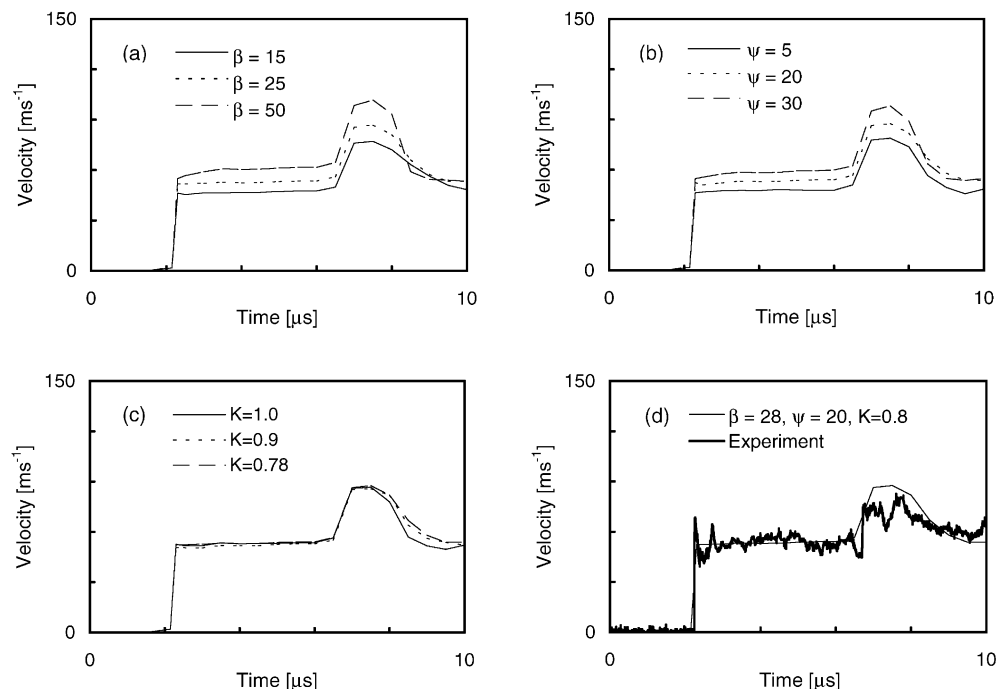


Fig. 5. A parametric study and determination of the material parameters for mortar based on the best fit of the free surface velocity, (a) effect of  $\beta$ , (b) effect of  $\psi$ , (c) effect of  $K$ , and (d) determination of best-fitting parameters ( $V_0 = 290 \text{ ms}^{-1}$ ).

three different values of  $K$  (0.78, 0.9, 1) with  $\beta = 28^\circ$  and  $\psi = 20^\circ$  follow each other closely. This is expected since this parameter characterizes the effect of stress state and the impact experiment involves mostly compressive loading with high triaxialities. Clearly, the friction angle  $\beta$  has the largest influence among the three parameters. Based on this analysis, a set of parameters that results in the best fit of the experiment is found to be  $\beta = 28^\circ$ ,  $\psi = 20^\circ$  and  $K = 0.8$ . The velocity profile calculated using this set of parameters is shown in Fig. 5(d) along with the measured velocity history. A good agreement is seen between the calculation and the experiment. This set of parameters is used for mortar in the remaining analyses.

Separate impact experiments were not conducted on the aggregate since a large enough piece of the granite is not available for testing. The calibration of the parameters for the aggregate phase uses the result of an impact experiment on concrete. This calibration process is similar to that for mortar except that the simulation conducted uses a micromechanical model for the concrete composite. While the calculation includes both mortar and aggregate, only the parameters for the aggregate are adjusted and the parameters for mortar determined above remain unchanged. Fig. 6 shows calculated and measured velocity profiles for an impact velocity of  $290 \text{ ms}^{-1}$ . The set of parameters for the aggregate that provides the best fit for the experiment is  $\beta = 22^\circ$ ,  $\psi = 17^\circ$  and  $K = 0.8$ . The corresponding profile is compared with the measured velocity history in Fig. 6(d).

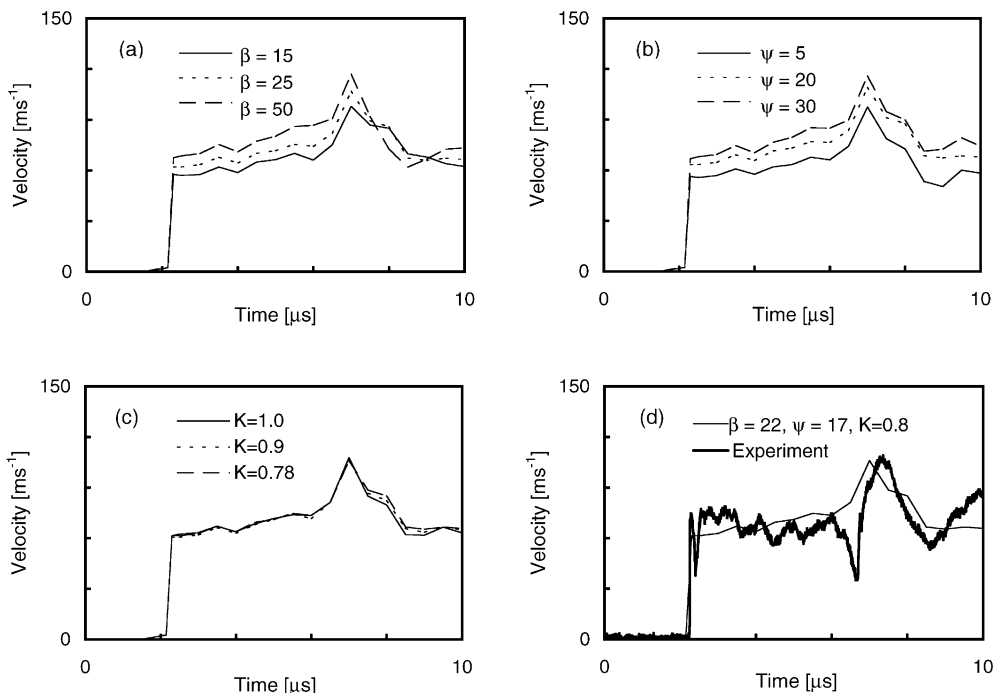


Fig. 6. A parametric study and determination of the material parameters for aggregate based on the best fit of the free surface velocity, (a) effect of  $\beta$ , (b) effect of  $\psi$ , (c) effect of  $K$ , and (d) determination of best-fitting parameters ( $V_0 = 290 \text{ ms}^{-1}$ ).

### 3. Numerical results

The numerical model described above is used to analyze the impact response of concrete. First, the predictive capability of the model is examined. To this end, the free surface velocity histories at the center of the target plate for two experiments with impact velocities of  $277 \text{ ms}^{-1}$  and  $330 \text{ ms}^{-1}$  are calculated. Note that the impact velocity for the experiment used for model calibration in Fig. 6 is  $290 \text{ ms}^{-1}$  or between the two impact velocities considered here. The calculated results are shown in Fig. 7 along with the measured profiles. The microstructure used in the calculations is (4) in Fig. 1. Since the distribution of phases in this microstructure may be different from those in the actual specimens of the two corresponding experiments, attention is not focused on the details of the oscillations of the velocity. Instead, the focus is on the average velocity and the overall history of velocity evolution. In both cases, the model prediction follows the measured response quite well.

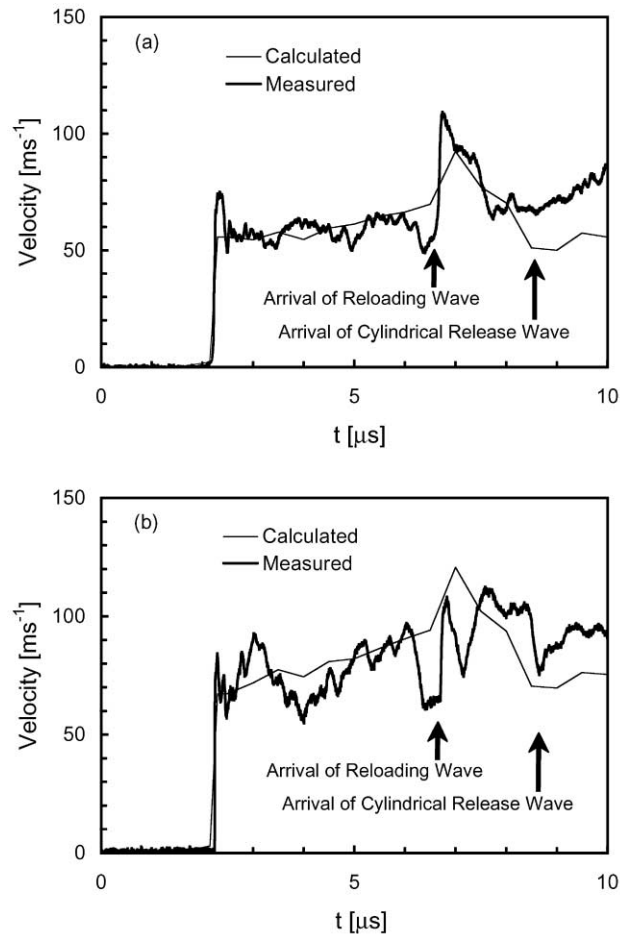


Fig. 7. Predicted and measured velocity profiles at the center of the rear surface of the anvil plate during plate impact on concrete; (a)  $V_0 = 277 \text{ ms}^{-1}$ , (b)  $V_0 = 330 \text{ ms}^{-1}$ .

The measured profiles show more fluctuations than the calculated profiles. This may be partly due to the material heterogeneities and porosity in each phase not explicitly accounted for by the numerical model. Also a 2D plane strain model is used. In these experiments, the phases have 3D morphologies. Nonetheless, the model tracks the overall trend and history of evolution fairly well. After the arrival of the reloading wave (indicated in Fig. 7), the calculated profiles deviate from the measured profiles. This deviation may be associated with the limitations of the constitutive model used in characterizing the part of the impact deformation that involves significant fragmentation and localized flow. In this paper, attention is focused on the response before the reloading wave arrives. Since good agreement with experiments is found for the range of impact velocity considered, an impact velocity of  $V_0 = 290 \text{ ms}^{-1}$  is used for the subsequent analyses which focus on the history of deformation and the effects of microstructure.

### 3.1. Microscopic deformation history

To illustrate the evolution of deformation at the microstructural level, the distributions of the volumetric strain rate ( $\dot{\epsilon}_{kk}$ ), hydrostatic pressure ( $p$ ), normal stress in the impact direction ( $\sigma_{22}$ ), elastic strain energy density ( $W^e$ ) and plastic work density ( $W^p$ ) at seven different times are shown in Figs. 8–10. All the contours are plotted on the deformed configurations. Time  $t = 0$  corresponds to the instant when the flying specimen comes into contact with the stationary anvil plate. Upon impact, compressive waves are generated at the contact faces. These waves propagate up in the specimen and down the anvil plate (not shown). Upon arriving at the free (top) surface of the specimen at approximately  $2.7 \mu\text{s}$ , the waves are reflected by the free surface back into the specimen, traveling downward toward the impact face as tensile waves. The tensile waves are superimposed on the upcoming compressive waves, reducing the stresses and strains in the material. This unloading process is completed at approximately  $5.4 \mu\text{s}$  after impact when the reflected tensile waves arrive at the impact face of the specimen. Subsequently, the specimen and the target separate and the impact loading on the specimen is terminated.

Fig. 8(a) shows that the magnitude of the volumetric strain rate along the loading wave front reaches  $10^5 \text{ s}^{-1}$  while the average strain rate is on the order of  $10^4 \text{ s}^{-1}$ . The figure well depicts the deformation history of the specimen at different stages of the impact event. The initial compressive waves are followed by the tensile waves reflected from the top free surface of the specimen. Tensile strains and stresses are denoted to be positive throughout the paper unless noted otherwise. It is interesting to note that even after the specimen is separated from the target at about  $5.4 \mu\text{s}$ , deformation continues due to waves trapped in the specimen. Also note that  $\dot{\epsilon}_{kk} \approx \dot{\epsilon}_{22}$  because  $\dot{\epsilon}_{33} = 0$  (plain strain) and  $\dot{\epsilon}_{11} \approx 0$  for most part of the specimen due to inertial constraint in the lateral direction.

Fig. 8(b) shows the evolution of the hydrostatic pressure in the specimen. The pressure varies with position and falls within the range of 1–1.5 GPa when the specimen is under full impact loading (at, say,  $t \approx 3 \mu\text{s}$ ). The confining pressure in the plate impact configuration does not come from physical boundary constraints but rather from the effect of inertia associated with the finite stress wave speed and the narrow time window with which the discussion is concerned. Specifically, the analysis focuses on the time period before unloading waves initiated from the outer periphery of the specimen arrive at the center [18]. Indeed, significant hydrostatic pressures exist in impact and penetration processes. For example, Forrestal and Tzou [13] studied the

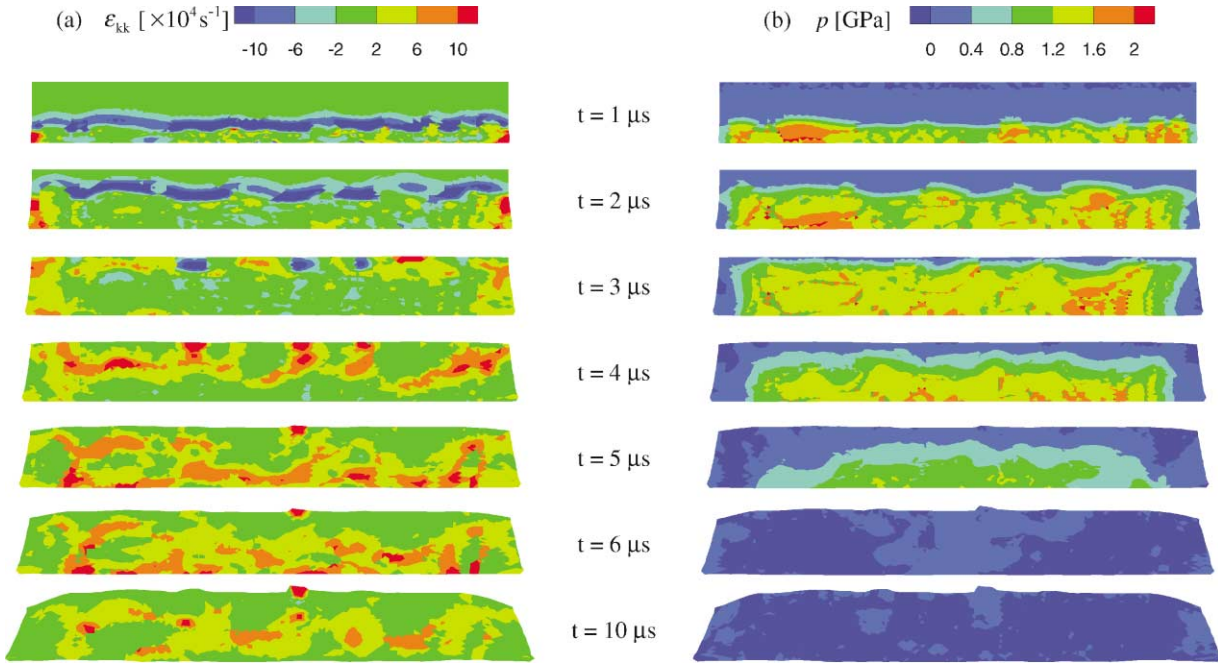


Fig. 8. Evolution of volumetric strain rate ( $\dot{\epsilon}_{kk}$ ) and hydrostatic pressure ( $p$ ) during impact of a concrete specimen against a steel plate ( $V_0 = 290 \text{ ms}^{-1}$ ).

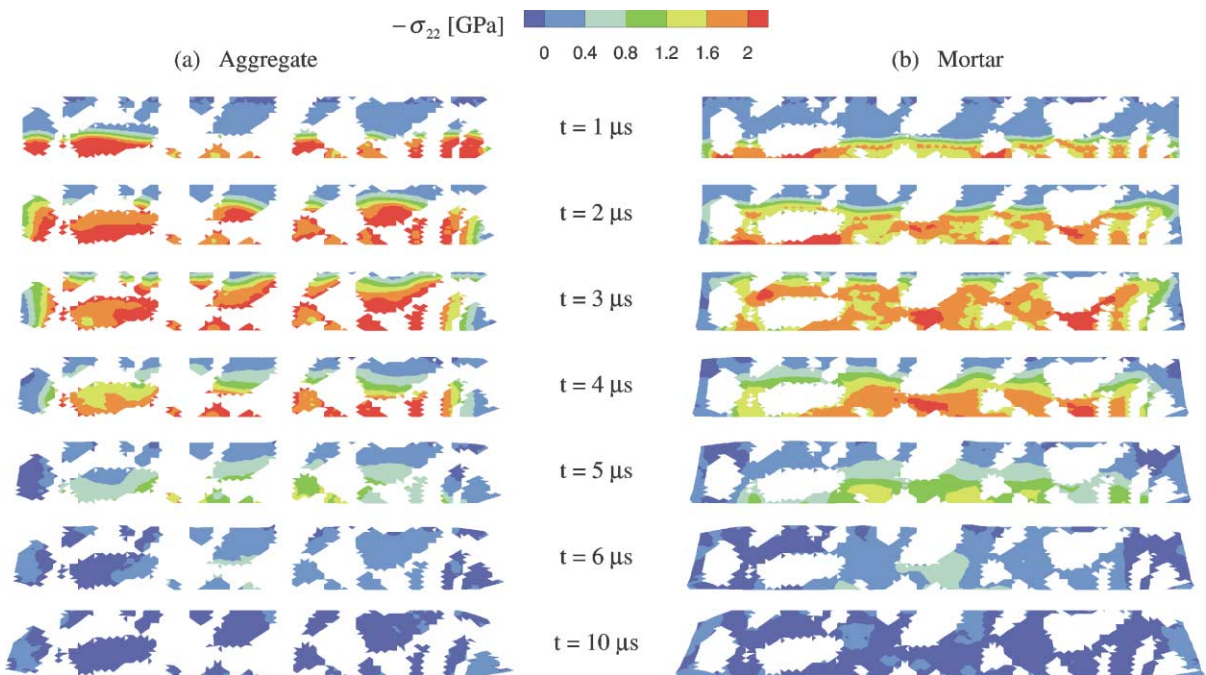


Fig. 9. Evolution of normal stress ( $\sigma_{22}$ ) during impact of a concrete specimen against a steel plate ( $V_0 = 290 \text{ ms}^{-1}$ ).

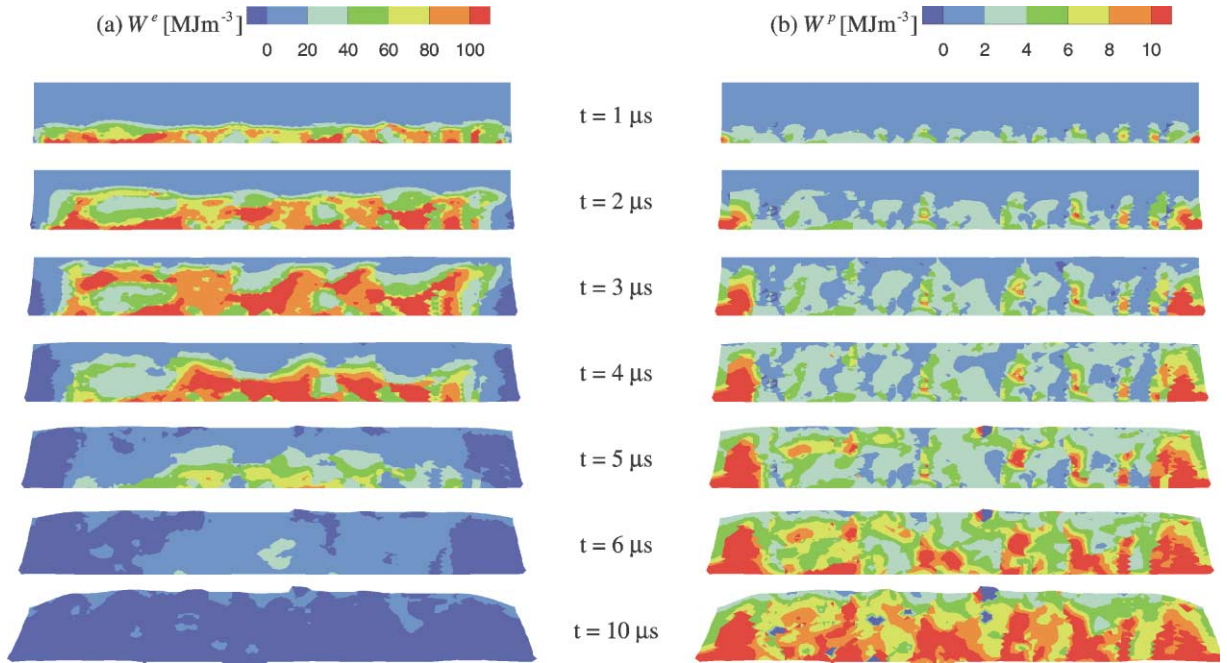


Fig. 10. Evolution of elastic strain energy density ( $W^e$ ) and plastic work density ( $W^p$ ) during impact of a concrete specimen against a steel plate ( $V_0 = 290 \text{ ms}^{-1}$ ).

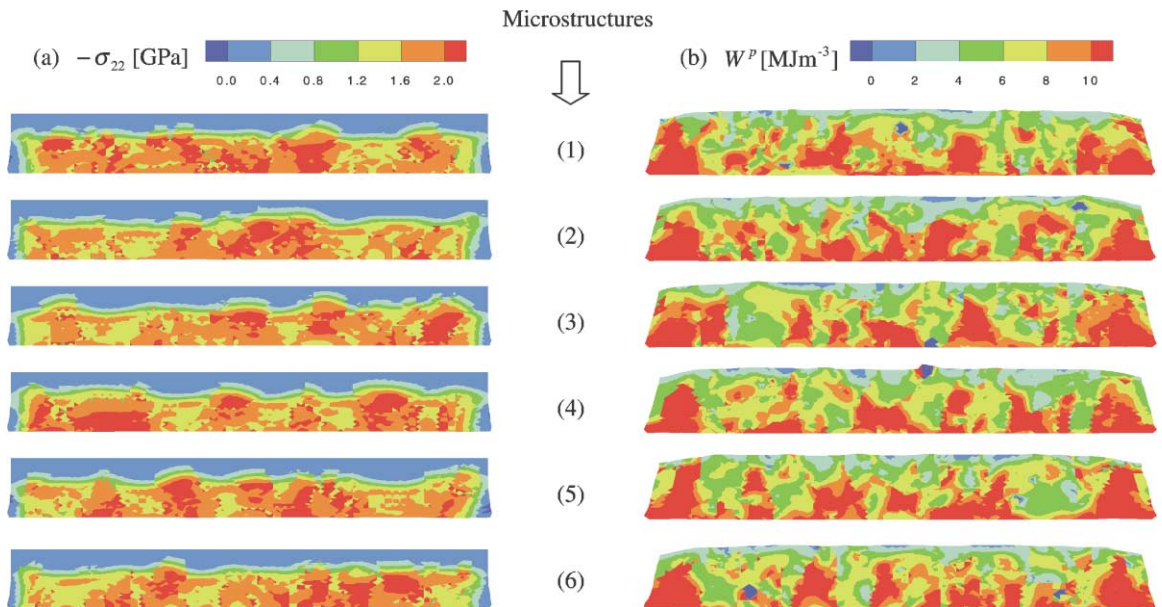


Fig. 11. Distribution of normal stress ( $\sigma_{22}$ ) at  $t = 2 \mu\text{s}$  and plastic work density ( $W^p$ ) at  $t = 7 \mu\text{s}$  in concrete specimens with different microstructures.

penetration of concrete targets and reported a confining pressure of 0.6 GPa at the ogive-nose tip of a steel projectile with a striking velocity of  $530 \text{ ms}^{-1}$ .

Fig. 8(b) also indicates that the transit time for wave propagation across the specimen is approximately  $2.7 \mu\text{s}$ . This duration compares reasonably well with the estimated time of  $2.54 \mu\text{s}$  obtained using the one-dimensional wave propagation theory and the effective, longitudinal wave speed of concrete calculated by

$$c_{\text{concrete}} = \sqrt{\frac{(1 - v_{\text{eff}})E_{\text{eff}}}{\rho_{\text{eff}}(1 + v_{\text{eff}})(1 - 2v_{\text{eff}})}}, \quad (18)$$

where  $E_{\text{eff}} = (1 - f)E_m + fE_g$ ,  $v_{\text{eff}} = (1 - f)v_m + fv_g$ , and  $\rho_{\text{eff}} = (1 - f)\rho_m + f\rho_g$ , with  $E$ ,  $v$ ,  $\rho$ , and  $f$  being Young's modulus, Poisson's ratio, mass density, and aggregate volume fraction, respectively. Subscripts  $m$  and  $g$  denote mortar and aggregate, respectively. An aggregate volume fraction of 42% and the material data for mortar and aggregate given in [18] are used. Ortiz [25] used the law of mixtures to describe the response of concrete in terms of the behaviors of its constituents. The distributions of  $p$  at  $t = 4$  and  $5 \mu\text{s}$  indicate that the unloading of the pressure in the specimen is slower than what is predicted by the one-dimensional wave propagation theory. This is due to the effects of the inelastic deformation that reduces the speed of wave propagation. Also, the material heterogeneities inherent in the concrete microstructure cause dispersion of the loading and unloading waves.

The distributions of normal stress,  $\sigma_{22}$ , in the aggregate and mortar phases are plotted separately in Fig. 9(a) and (b), respectively, for clear visualization of the stress variation in each phase and the phase morphology. Overall, the two phases sustain similar levels of stress and the distributions appear to be continuous across the phase interfaces. It is known that quasistatically applied stresses distribute unequally between mortar and aggregate and a state of uniaxial compressive loading results in significantly large transverse splitting stresses in mortar [25–27]. However, our simulations indicate that under high-strain-rate dynamic loading in a plain-strain configuration both phases of concrete sustain almost the same levels of compressive stresses. This can be attributed to limited stress redistribution between the two phases due to lateral inertial confinement. The average stresses carried by both aggregate and mortar are on the order of 1.6 GPa. Echoing what was observed in experiments [18], the stress sustained by the material in the loading direction ( $\sigma_{22}$ ) is much higher than the quasistatic strength of unconfined concrete (30 MPa). This dramatic increase is partly due to the much higher hydrostatic pressures that exist in the impact process and partly due to the strain-rate hardening effect. Recall that there is no lateral confining stress in the quasistatic compression test and the split Hopkinson bar test. Moreover, they involve strain rates on the order of  $10^{-3}$  and  $10^2$ – $10^3 \text{ s}^{-1}$ , respectively.

The energy absorbency and dissipation capacities of concrete are of interest in impact and penetration. To analyze the evolution of the elastic energy stored in the specimen and plastic work dissipated through irreversible plastic deformation, the elastic strain energy density ( $W^e = \int_0^t \boldsymbol{\tau} : \mathbf{D}^e dt$ ) and plastic work density ( $W^p = \int_0^t \boldsymbol{\tau} : \mathbf{D}^p dt$ ) are computed and plotted for seven different times in Fig. 10. During the loading and unloading process, the strain energy density undergoes a storing and release cycle. The strain energy stored is the highest between  $2.7$ – $2.9 \mu\text{s}$ . It decreases thereafter with the unloading of the specimen when it is converted into kinetic energy and

dissipated through plastic work. It can be seen that more strain energy is stored in the mortar than in the aggregate, (compare Figs. 4 and 10 for distribution of phases). This is in spite of the higher stresses in the aggregate. The lower elastic modulus of the mortar allows larger elastic strains to occur and more elastic energy to be stored in it. The plots also illustrate the effect of cylindrical unloading waves that propagate from the lateral free surface towards the center of the specimen. The density of plastic work increases monotonically with time as plastic deformation progresses. Although mortar generally undergoes larger plastic deformation than aggregate, the levels of work dissipation are comparable for both phases. The regions in the vicinity of the lateral free surfaces undergo greater plastic deformations due to the lack of lateral confinement and the lower hydrostatic pressures. Fig. 10(a) and (b) indicate that the average level of plastic work density at  $t = 10 \mu\text{s}$  is roughly 20% of the peak average elastic strain energy density at  $t = 3 \mu\text{s}$ . As discussed later, numerical simulations predict that approximately 17% of the input energy is absorbed by concrete through plastic dissipation at  $V_0 = 290 \text{ms}^{-1}$  for the duration analyzed.

### 3.2. Effect of microstructural morphology

The arbitrary distribution of phases in the microstructure of concrete poses a challenge to the characterization of deformation. The micromechanical model used in the current analyses requires the explicit use of samples of microstructures. Since the characteristic length in the microstructure (e.g. the average aggregate size) is a significant fraction of the specimen thickness (10 mm) used in both the experiments and the simulations, a question arises as to how representative the result of a particular simulation is using a specific sample of microstructure. While it is not of much practical significance to concentrate on the specific value of a field quantity at specific points because of the material inhomogeneities, general characteristics of the deformation field are of special interest. These characteristics include the average stress level and the amplitude of spatial variation. To analyze the effect of microstructural morphology on the results of numerical simulations, a series of calculations are carried out using the six different random samples of microstructure shown in Fig. 1. Calculations using these six microstructures have otherwise the same loading and geometric conditions. Fig. 11 compares the results of these calculations. The distributions of  $\sigma_{22}$  at  $t = 2 \mu\text{s}$  and distributions of the plastic work density at  $t = 7 \mu\text{s}$  for each of the six cases are shown. The time  $t = 2 \mu\text{s}$  is in the loading stage of the deformation and the time of  $t = 7 \mu\text{s}$  is chosen so that the plastic work density over a longer period of time can be examined. It can be seen that the results are very similar to each other in terms of the level of stress and amount of plastic work in each phase. The stress in the inclusions is consistently higher than that in the matrix. Clearly, the six sets of results are consistent with each other and are equivalent in terms of the average values of stress and deformation patterning.

To provide a quantitative comparison of the average stresses carried by the six specimens, the history of particle velocity at the center of the free surface of the target plate is shown in Fig. 12(a) for each microstructure. An average measure for the normal stress  $\sigma_{22}$  at the specimen/target interface is obtained from Eq. (17) and is also shown in this figure. The oscillations in the profiles are caused by material inhomogeneities in the microstructures. The specific pattern of oscillations

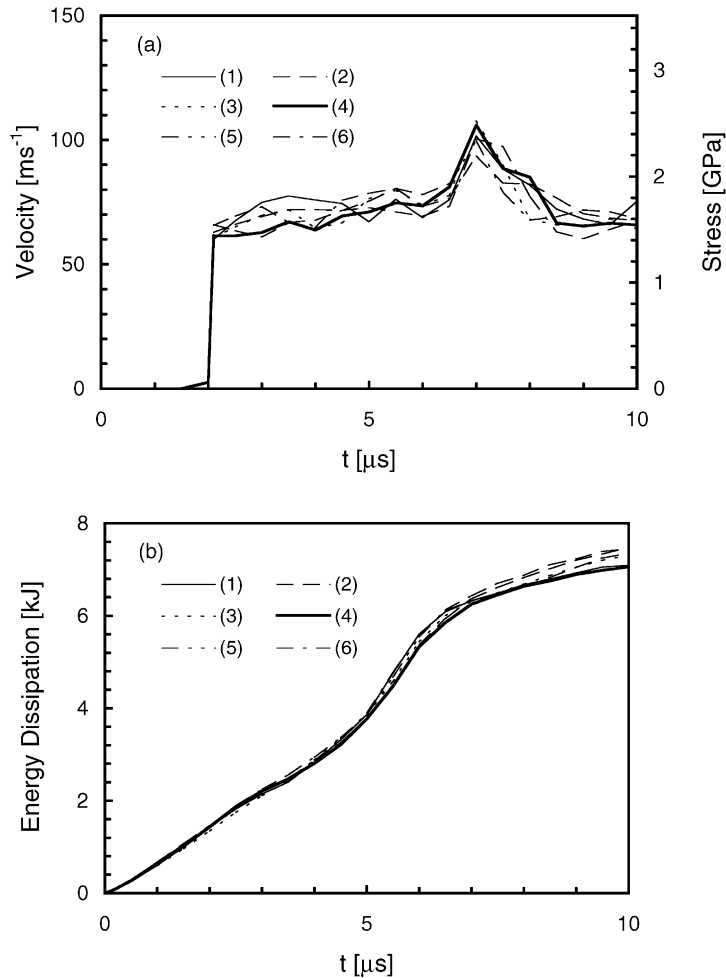


Fig. 12. Effect of different concrete microstructures on (a) the free surface velocity of the anvil plate ( $V_{fs}$ ) and the interpreted normal stress ( $\sigma_{22}$ ), and (b) the total energy dissipated through plastic deformation of concrete ( $\Omega^P$ ). Note that  $t = 0$  in (b) corresponds to the instant of impact and coincides with  $t \approx 2$  in (a).

is related to random phase distribution in each microstructure, causing the peaks and valleys to occur arbitrarily in each case. However, it is clear that the average velocity ( $\approx 70 \text{ ms}^{-1}$ ) and consequently stress carried by the specimen ( $\approx 1.6 \text{ GPa}$ ) is essentially the same for all cases analyzed. Also, the level of oscillations ( $\pm 10 \text{ ms}^{-1}$  for the velocity and  $\pm 0.2 \text{ GPa}$  for the stress) are similar for all cases. Therefore, it can be concluded that the random sampling of microstructural morphology does allow the simulations to capture the average stress-carrying capability of the concrete under the conditions of the impact experiments. The calculation with a particular choice of microstructure can also reveal the amount of velocity and stress oscillations at a certain distance away from the impact face.

The history of total plastic work,  $\Omega^P = \int_V \int_0^t \boldsymbol{\tau} : \mathbf{D}^P dt dV$ , for each of the six specimens is shown in Fig. 12(b). At  $t = 10 \mu\text{s}$ , the total plastic work is in the range of 7–7.5 kJ which constitutes

approximately 17% of the total input energy (43 kJ). The total plastic dissipation does not vary significantly among the microstructures throughout the impact process. The largest deviation is approximately 6%, occurring at the end of the time period analyzed. This lack of difference among the six cases analyzed again points out that the overall behavior of concrete is well captured by any particular choice of microstructural sample in the plate impact experiments described in [18] and in numerical simulations of the experiments discussed in this paper. This finding is in spite of the fact that the deformation states at particular material points are significantly influenced by the microstructural phase distributions, providing credence to the approach taken and the analyses carried out.

### 3.3. Effect of aggregate volume fraction

The aggregate in concrete provides reinforcement and thus enhances the strength of concrete. The authors are unaware of any quantitative characterizations of this strengthening effect under dynamic loading conditions published in the literature. The micromechanical model used here allows the effect of the aggregate to be explicitly delineated. A series of calculations are carried out using microstructures with a range of aggregate volume fraction. Shown in Fig. 13, these microstructures have similar grain morphologies which are variations from that in the fourth

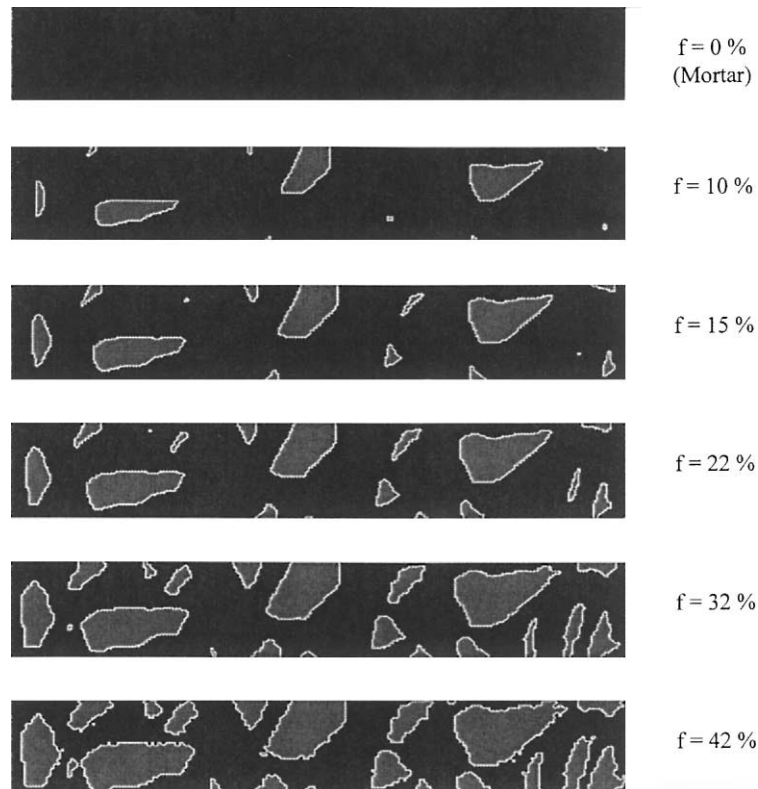


Fig. 13. Microstructures with different aggregate volume fractions considered in the study.

microstructure of Fig. 1. Having aggregate volume fractions between 0% and 42%, the six microstructures are obtained by successively converting layers of the aggregate material on each grain of aggregate into the matrix material. This successive process produced varying degrees of aggregate volume fraction between 0% (representing pure mortar) and 42% which is the same as that for the microstructures in Fig. 1.

The distributions of the longitudinal stress  $\sigma_{22}$  at  $t = 2 \mu\text{s}$  and the plastic work density  $W^P$  at  $t = 7 \mu\text{s}$  for the six cases are shown in Fig. 14. It can be seen that higher volume fractions give rise to higher  $\sigma_{22}$  or higher dynamic load-carrying capacity for the concrete. Although the plastic dissipation is not uniform throughout a specimen, the overall plastic work absorbed by a specimen also increases with increasing aggregate volume fraction, as indicated by the size of areas by  $W^P$  distributions in Fig. 14. To obtain quantitative measures of these effects, the histories of the particle velocity at the center of the free surface of the target plate for the six cases are shown in Fig. 15(a) and the corresponding histories of the total plastic work ( $\Omega^P$ ) are shown in Fig. 15(b). Clearly, higher aggregate volume fractions give rise to higher velocities and therefore higher average stresses carried by the specimens. This enhancement is approximately 30% (from 1.2 to 1.6 GPa) for a volume fraction increase from 0% to 42%. This result is consistent with the amount of increase in velocity and stress observed in the experiments [18]. Note that the velocity profiles show more fluctuations at higher grain volume fractions reflecting increasing level of material heterogeneity in the microstructure. The benefit of the addition of aggregate into the matrix regarding energy dissipation is also clear. Fig. 15(b) shows that  $\Omega^P$  increases significantly with increasing aggregate volume fraction. At  $10 \mu\text{s}$  after impact, the dissipation for the microstructure with 42% aggregate is 15% higher than that for pure mortar (an increase from 6.2 to 7.1 kJ). The

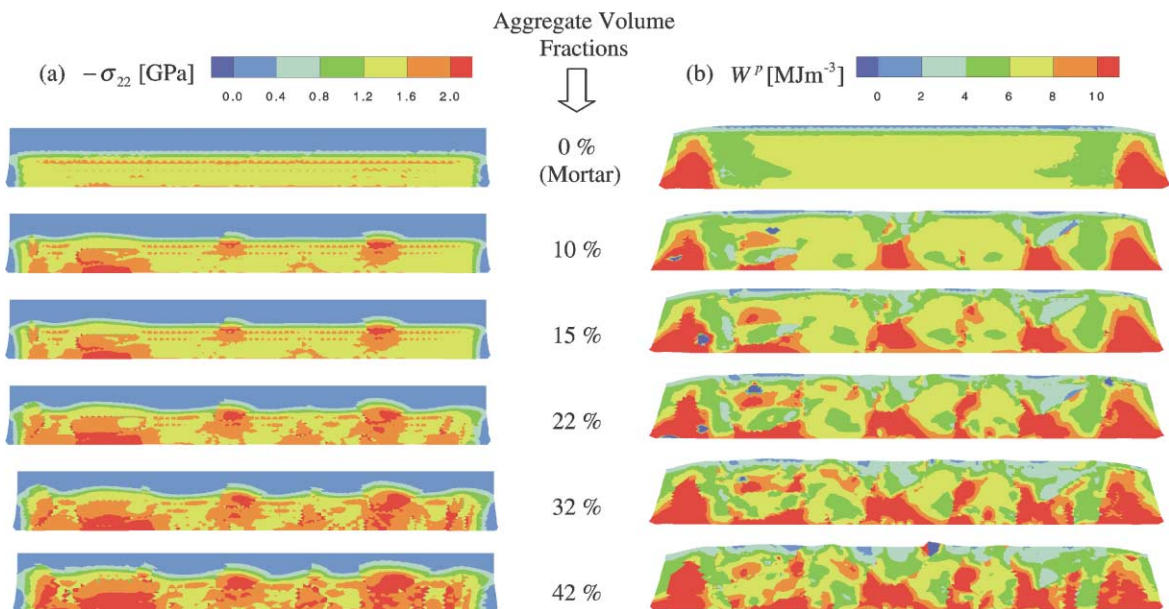


Fig. 14. Distribution of normal stress ( $\sigma_{22}$ ) at  $t = 2 \mu\text{s}$  and plastic work density ( $W^P$ ) at  $t = 7 \mu\text{s}$  in concrete specimens with different aggregate volume fractions.

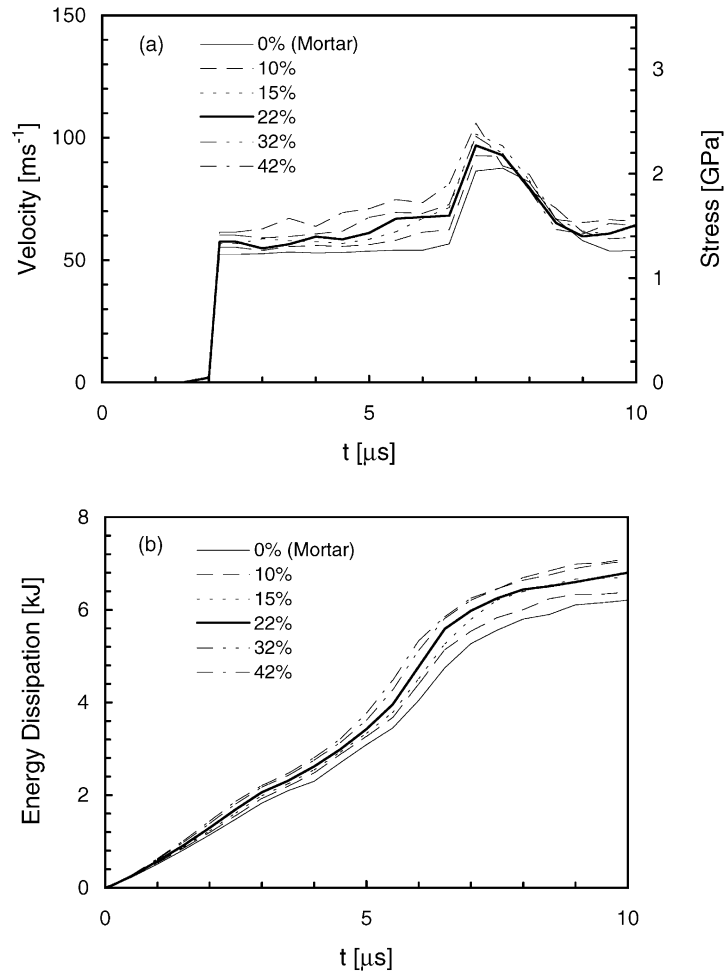


Fig. 15. Effect of different aggregate volume fractions on (a) the free surface velocity of the anvil plate ( $V_{fs}$ ) and the interpreted normal stress ( $\sigma_{22}$ ), and (b) the total energy dissipated through plastic deformation of concrete ( $\Omega^p$ ).

higher energy absorbency comes from two sources. First, the introduction of the stronger phase strengthens the materials, causing the mechanical work to be higher for a given amount of deformation. Second, material inhomogeneities promote nonuniform deformation and increases local strains. This effect is especially pronounced in the weaker phase. Consequently, more energy is dissipated through the larger deformations.

#### 4. Conclusions

This paper provides an analysis and characterization of the dynamic, high strain rate behavior of concrete and mortar observed in the experimental part of the investigation [18]. The conditions involve strain rates on the order of  $10^4 \text{ s}^{-1}$  and hydrostatic pressures of up to 1.5 GPa. A

micromechanical model that provides explicit account for the arbitrary microstructural phase morphologies of concrete is formulated. Microstructural morphologies in actual specimens used in experiments are digitized and used. This framework of analysis allows the effect of microstructure and the properties of the mortar and aggregate phases to be explored. A fully dynamic finite element formulation is used, accounting for the effect of inertia on the transient material response and deformation. An extended Drucker–Prager constitutive law is used to describe the behavior of the two constituent phases, providing a phenomenological account for the dependence of flow stress on internal friction through pressure, strain hardening/softening, and strain rate sensitivity. The material parameters in the constitutive model, valid for the high strain rate/high pressure conditions analyzed, are determined directly from impact and split Hopkinson bar experiments reported in the experimental part of this investigation and from a parametric study using independent impact experiments.

The analysis focuses on the response of concrete and mortar in a plate impact configuration for which experimental data are available for direct comparison. Numerical simulations show that an average confining pressure of 1.2 GPa develops during planar impact between concrete flyers and steel targets due to the effect of inertia. Strain rates in impacted specimens are on the order of  $10^4 \text{ s}^{-1}$ . The high pressures and high strain rates combine to allow extremely high levels of stresses to be sustained in the concrete specimens for short durations. At an impact velocity of  $290 \text{ ms}^{-1}$ , the normal stresses carried by concrete are on the order of 1.6 GPa, consistent with experimental measurements. The calculations also show that random samples of microstructural morphologies allow reasonably representative results to be obtained from simulations concerning the histories of stress carried by impacted specimens and the energy absorbency of concrete. The effects of aggregate volume fraction on stress-carrying capacity and energy absorbency are analyzed and characterized. When the volume fraction is increased from 0% to 42%, an increase of approximately 30% in average stress and an increase of 15% in energy dissipation are found.

A two-dimensional, plane-strain model of the material microstructure is used. The framework and approach used here can be applied together with a full three-dimensional model accounting for the 3D phase distributions in microstructure. Such a model may improve the accuracy of the simulations in capturing the level of fluctuations in the velocity profiles. Indeed, the calculated profiles show less fluctuations than the measured profiles. However, 3D simulations would require substantially more computational resources. The 2D model used in this paper has yielded result that are in good agreement with experimental measurements in terms of average stresses and the effect of aggregate on flow stress. This model also allows the effects of microstructural variations in grain size, grain volume fraction, phase morphology and phase constitutive behavior to be explored.

## **Acknowledgements**

This research is sponsored by the US Air Force Office of Scientific Research under grants F49620-97-10055, F49620-97-1-0415 and F08671-98009587. Computations reported are carried out on Cray Supercomputers at the San Diego Supercomputer Center, Jet Propulsion Lab and the Naval Oceanographic Office (NAVOCEANO) Major Shared Resource Center (MSRC).

## References

- [1] Chen WF, Saleeb AF. Constitutive equations for engineering materials, Vol. 1: Elasticity and modeling. New York: Wiley, 1982.
- [2] Ortiz M. An analytical study of the localized failure modes of concrete. *Mech Mater* 1987;6:159–74.
- [3] Rashid Y. Analysis of prestressed concrete pressure vessels. *Nucl Eng Des* 1968;7(4):334–55.
- [4] Bazant ZP, Oh B-H. Crack band theory for fracture of concrete. *RILEM Mater Struct* 1983; 16: 155-177.
- [5] Beshara F, Virdi K. Prediction of dynamic response of blast-loaded reinforced concrete structures. *Comput Struct* 1992;44(1/2):297–313.
- [6] Soroushian P, Choi K-B, Alhamad A. Dynamic constitutive behavior of concrete. *ACI J* 1986;83:251–9.
- [7] Beshara F. Smearred crack analysis for reinforced concrete structures under blast-type loading. *Eng Fract Mech* 1993;45(1):119–40.
- [8] Shirai K, Ito C, Onuma H. Numerical studies of impact on reinforced concrete beam of hard missile. *Nucl Eng Des* 1994;150:483–9.
- [9] Tedesco JW, Hughes ML, Ross CA. Numerical simulation of high strain rate concrete compression tests. *Comput Struct* 1994;51(1):65–77.
- [10] Tedesco JW, Powell JC, Ross CA, Hughes ML. A strain-rate-dependent concrete material model for ADINA. *Comput Struct* 1997;64(5/6):1053–67.
- [11] Moxley RE, Adley MD, Rohani B. Impact of thin-walled projectiles with concrete targets. *Shock Vibration* 1995;2(5):355–64.
- [12] Berger RP, Adley MD. Two-dimensional projectile penetration into curvilinear geologic/structural targets: PENCURV. Proceedings of the 65th Shock and Vibration Symposium. San Diego, CA, 1994.
- [13] Forrestal MJ, Tzou DY. A spherical cavity-expansion penetration model for concrete targets. *Int J Solids and Struct* 1997;34(31-32):4127–46.
- [14] Cela JLL. Analysis of reinforced concrete structures subjected to dynamic loads with a viscoelastic Drucker–Prager model. *Appl Math Modell* 1998;22:495–515.
- [15] Sawamoto Y, Tsubota H, Kasai Y, Koshika N, Morikawa H. Analytical studies on local damage to reinforced concrete structures under impact loading by discrete element method. *Nucl Eng Des* 1998;179:157–77.
- [16] Riera JD, Iturriz I. Discrete elements model for evaluating impact and impulsive response of reinforced concrete plates and shells subjected to impulsive loading. *Nucl Eng Des* 1998;179:135–44.
- [17] Magnier SA, Donze FV. Numerical simulations of impacts using a discrete element method. *Mech Cohesive-Frictional Mater* 1998;3(3):257–76.
- [18] Grote DL, Park SW, Zhou, M. Dynamic behavior of concrete at high strain rates and pressures: I. Experimental characterization. *Int J Impact Eng* 2001;25(3):869–86.
- [19] Desai CS, Siriwardane HJ. Constitutive laws for engineering materials. Englewood Cliffs, NJ: Prentice-Hall, 1984.
- [20] Drucker DC, Prager W. Soil mechanics and plastic analysis or limit design. *Quart Appl Math* 1952;10:157–65.
- [21] Hofstentter G, Taylor RL. Non-associative Drucker–Prager plasticity at finite strains. *Appl Numer Methods* 1990;6:583–9.
- [22] Famiglietti CM, Prevost JH. Solution of the slump test using a finite deformation elasto-plastic Drucker–Prager model. *Int J Numer Methods Eng* 1994;37:3869–903.
- [23] Nemat-Nasser S. On behavior of granular materials in simple shear. *Soils Found* 1980;20(3):59–73.
- [24] Divakar MP, Fafitis A, Shah SP. Constitutive model for shear transfer in cracked concrete. *J Struct Eng* 1987;113(5):1046–62.
- [25] Ortiz M. A constitutive theory for the inelastic behavior of concrete. *Mech Mater* 1985;4:67–93.
- [26] Ortiz M, Popov EP. A physical model for the inelasticity of concrete. *Proc Roy Soc. London* 1982;A383:101–25.
- [27] Ortiz M, Popov EP. Plain concrete as a composite material. *Mech Mater* 1982;1:139–50.